

# **The effect of deposition energy on the growth and structure of ultrathin amorphous carbon films synthesized by energetic atoms examined by molecular dynamics simulations**

N. Wang and K. Komvopoulos\*

*Department of Mechanical Engineering, University of California, Berkeley, California 94720, USA*

## **Abstract**

The growth process of ultrathin amorphous carbon films was investigated by molecular dynamics simulations based on the second-generation reactive-empirical-bond-order potential. Films with different structures were simulated by varying the carbon atom energy in the range of 1–120 eV. Film intrinsic properties, such as density and residual stress, were determined after the system reached equilibrium. Carbon atom short- and intermediate-range ordering was studied in terms of atomic hybridization and ring connectivity simulation results. A multilayer film structure comprising intermixing layer, bulk film, and surface layer was observed for relatively high deposition energy, in agreement with the classical subplantation model. The highest film density (3.3 g/cm<sup>3</sup>), *sp*<sup>3</sup> fraction (~43%), and carbon atom intermediate ordering were found for a deposition energy of ~80 eV, which is in good agreement with experimental findings.

---

\*Corresponding author:

K. Komvopoulos: Tel.: 510-642-2563, Fax: 510-642-5539, E-mail: kyriakos@me.berkeley.edu

## I. Introduction

Amorphous carbon (*a*-C) films with high  $sp^3$  fractions demonstrate unique characteristics, such as high hardness, low friction, good wear resistance, and high chemical inertness.<sup>1-6</sup> Many efforts have been made to enhance the quality of *a*-C films by varying the deposition method and process parameters.<sup>7-8</sup> Although traditional deposition techniques, such as plasma-enhanced chemical vapor deposition and sputtering, have been used to deposit *a*-C films with unique physical properties, energetic deposition methods, in particular, filtered cathodic vacuum arc (FCVA) deposition, has captured significant research attention in recent years interest because the highly ionized plasma, intrinsic of FCVA, results in the formation of hard, dense, continuous, and smooth ultrathin carbon films.<sup>5,9-10</sup>

The ion energy effect on the properties of *a*-C films deposited by the FCVA method has been the main objective of several studies.<sup>1,11-14</sup> The formation of *a*-C films with a high content of  $sp^3$  hybridization can be explained by the subplantation model,<sup>15</sup> which postulates that energetic ions penetrating the surface of the bombarded material introduce local compressive stresses that promote  $sp^3$  formation. Because of the subplantation effect, FCVA-deposited films exhibit multilayer structure.<sup>16-18</sup> However, limitations in the signal-to-noise ratio of characterization methods present an obstacle in understanding the formation of nanometer-thick films.

Molecular dynamics (MD) provides an alternative method for studying ultrathin film growth. MD provides an atomistic perspective of the material behavior and a statistical description of material response. Kaukonen and Nieminen<sup>19</sup> used the Tersoff potential<sup>20,21</sup> to simulate *a*-C film growth for carbon atom energy in the range of 1–70 eV and observed dense film formation for carbon atom energies between 40 and 70 eV. Marks et al.<sup>22</sup> used the Stillinger and Weber potential<sup>23</sup> to perform two-dimensional MD simulations and reported a transition from tensile to compressive residual stress with increasing deposition energy  $E_d$ , and a maximum compressive stress for a  $E_d \approx 30$  eV, which is less than what has been observed in experimental studies.<sup>11-14</sup> Jager and Albe<sup>24</sup> compared the Tersoff and reactive-empirical-bond-order (REBO) potential<sup>25-27</sup> by simulating ion-beam deposition of *a*-C films and proposed a modified REBO potential for simulating the film deposition process, which was used in MD simulations

of Ma et al.<sup>28</sup> to study the microstructure and internal stress of ultrathin *a*-C films. Results from the latter study revealed that incident carbon atoms caused reconstruction of the substrate surface, leading to the formation of a three-layer structure comprising the substrate, an intermixing layer, and the deposited film, in agreement with the subplantation model.

Similar to other amorphous structures, *a*-C lacks long-range order. While the majority of previous studies have focused on *a*-C short-range order (e.g.,  $sp^3$  and  $sp^2$  hybridization),<sup>19,22,24,28,29</sup> insight into intermediate-range order (i.e., length scale of one to two times the average bond length) is limited. Intermediate-range order is considered to control the mechanical, optical, and electrical properties of amorphous materials.<sup>30,31</sup> Although some experimental measurements, such as Raman shift, may provide information about intermediate-range order (e.g., clustering), MD simulations can provide much more detailed information, which is cumbersome or impossible to experimentally deduce.<sup>32,33</sup> The main objective of this study is to elucidate the dependence of short- and intermediate-range order in *a*-C films on incidence atom energy. Because previous studies<sup>11-14</sup> have shown that the optimal incidence energy for *a*-C film deposition is ~80–100 eV, MD simulation results are presented for  $E_d$  in the range of 1–120 eV.

## II. MODELING AND NUMERICAL PROCEDURES

### A. Molecular dynamics simulations

MD analysis relies on Newton's second law to simulate the motion of atoms. Essential to this method is the interaction force between atoms, represented by an interaction potential in MD studies.<sup>34</sup> The second-generation REBO potential<sup>25-27,35</sup> is adopted in this study because it is the most often used and acclaimed potential for hydrocarbon-related studies. The velocity-Verlet method<sup>36</sup> is used to integrate Newton's second law in the present MD analysis, which uses the large-scale atomic/molecular massively parallel simulator (LAMMPS).<sup>37</sup>

The origin of the second-generation REBO potential can be traced back to the Tersoff potential,<sup>20,21</sup> which is applicable to systems of atoms interacting with each other through covalent bonds, such as carbon and silicon atoms. The potential energy associated with each bond consists of two parts

representing attractive and repulsive energy terms. The influence of a third atom on a given bond is taken into account through a correction factor. The Tersoff potential energy of a system  $E$  is expressed as

$$E = \frac{1}{2} \sum_i \sum_{j \neq i} V_{ij} \quad (1)$$

where  $V_{ij}$  is the potential energy associated with the bond of two atoms  $i$  and  $j$ , given by

$$V_{ij} = f_C(r_{ij})[f_R(r_{ij}) - B_{ij}f_A(r_{ij})] \quad (2)$$

where  $f_R$  and  $f_A$  represent repulsive and attractive potentials, respectively, given by  $f_R(r) = A \exp(-\lambda_1 r)$  and  $f_A(r) = \bar{A} \exp(-\lambda_2 r)$ ,<sup>20,21</sup> and  $B_{ij}$  represents the effect of a third atom close to atom  $i$ . Because a covalent bond can only form when two atoms are close to each other and the bond also prevents the two atoms from approaching each other beyond a certain distance, the distance  $r$  between the two atoms (bond length) is in a narrow distance range. To account for this effect, a cut-off distance function  $f_C(r)$  is included the interatomic potential  $V_{ij}$ , which is given by<sup>20,21</sup>

$$f_C(r) = \begin{cases} 1 & r < R_1 \\ \frac{1}{2} \left[ 1 - \cos \left( \frac{\pi(r - R_1)}{R_2 - R_1} \right) \right] & R_1 < r < R_2 \\ 0 & r > R_2 \end{cases} \quad (3)$$

Coefficient  $B_{ij}$  is expressed as<sup>20,21</sup>

$$B_{ij} = \left[ 1 + \beta^n \zeta_{ij}^n \right]^{-1/(2n)}$$

where

$$\zeta_{ij} = \sum_{k \neq i, j} f_C(r_{ik}) g(\theta_{ijk}) \exp[\lambda_3^m (r_{ij} - r_{ik})^m] \quad (4)$$

and

$$g(\theta) = \gamma_{ijk} \left( 1 + \frac{c^2}{d^2} - \frac{c^2}{[d^2 + (\cos \theta - \cos \theta_0)^2]} \right)$$

Parameters  $R_1$ ,  $R_2$ ,  $A$ ,  $\bar{A}$ ,  $\beta$ ,  $\lambda_1$ ,  $\lambda_2$ ,  $\lambda_3$ ,  $m$ ,  $n$ ,  $c$ ,  $d$ ,  $\gamma_{ijk}$ , and  $\theta_0$  included in equations are quoted from the literature.<sup>21</sup>

Although the Tersoff potential can be used to describe single, double, and triple bonds, it cannot be used to describe  $\pi$  and conjugated bonds. To overcome this limitation, Brenner<sup>25,26</sup> modified the

Tersoff potential to include the conjugation effect, introducing the so-called first-generation REBO potential. The main difference between the Tersoff potential and the first-generation REBO potential is that the latter accounts for the effect of nearby atoms on the bond of atoms  $i$  and  $j$ , which is represented by coefficient  $b_{ij}$ . In addition to the effect of atoms near atom  $i$ , the effect of atoms close to atom  $j$  is also included in the first-generation REBO potential. The conjugation function  $B_{ij}$  is given by<sup>25</sup>

$$B_{ij} = \frac{1}{2}(b_{ij} + b_{ji}) + F_{ij}(N_i^t, N_j^t, N_{ij}^{conj}) \quad (5)$$

where

$$b_{ij} = \left[ 1 + H_{ij}(N_i^h, N_i^c) + \sum_{k \neq i, j} f_C(r_{ik}) g(\theta_{ijk}) \exp[\alpha_{ijk} [(r_{ij} - R_{ij}^e) - (r_{ik} - R_{ij}^e)]] \right]^{-\delta_i} \quad (6)$$

where  $N_i^h$ ,  $N_i^c$ , and  $N_i^t$  are the number of hydrogen atoms, the number of carbon atoms, and the total number of atoms bonded to the atom  $i$ .  $H_{ij}$  and  $F_{ij}$  are obtained from bicubic and tricubic splines of known values for integer numbers of  $N_i^h$ ,  $N_i^c$ ,  $N_i^t$ , whereas  $N_i^{conj}$ ,  $\alpha_{ij}$ ,  $R_{ij}^e$ , and  $\delta_i$  are fitting parameters obtained from previous studies.<sup>25,26</sup>

The first-generation REBO potential has been widely used to model hydrocarbon systems.<sup>24,28</sup> However, because the repulsive and attractive potentials are too restrictive for modeling energetic atomic collisions, Brenner<sup>27</sup> modified this potential to overcome this problem, introducing a new potential known as the second-generation REBO potential. This potential also increased the accuracy of  $H_{ij}$  and  $F_{ij}$  through the use of more accurate values for the integer numbers  $N_i^h$ ,  $N_i^c$ ,  $N_i^t$  and  $N_i^{conj}$ . The estimate of the correction factor  $B_{ij}$  was also improved by using more accurate values to fit  $H_{ij}$  and  $F_{ij}$ . The second-generation REBO potential is used in this study to describe the interaction between carbon atoms.

Jager et al.<sup>24</sup> used the first-generation REBO potential to perform MD simulations of the deposition of a carbon film, but although they obtained a film density close to that of diamond, the  $sp^2$  content was ~90%, which is close to that of graphite. Thus, to simulate the formation of a carbon film with a high  $sp^3$  content, they increased the cut-off distance  $R_1$ , and  $R_2$  in Eq. (4) from 1.7 and 2.0 Å to 1.95 and 2.25 Å, respectively. While this resulted in the simulation of a carbon film with an extremely

high  $sp^3$  content (>85%), these changes in the cut-off distance also led to the formation of non-physical structures.<sup>38</sup> In the present study, the second-generation REBO potential and the LAMMPS code<sup>37</sup> were used to study the film deposition process. A total of 1400 carbon atom depositions were simulated sequentially to simulate the formation of a carbon film.

The film stress is calculated from a per-atom tensor  $S_{ab}$ , which includes kinetic, pairwise, and bond energy contributions (therefore, has units of stress  $\times$  volume), defined as

$$S_{ab} = -[mv_a v_b + \frac{1}{2} \sum_{n=1}^{N_p} (r_{1a} F_{1b} + r_{2a} F_{2b}) + \frac{1}{2} \sum_{n=1}^{N_b} (r_{1a} F_{1b} + r_{2a} F_{2b})] \quad (7)$$

where the first term represents the contribution of kinetic energy, the second term is a pairwise energy contribution with a total number of loops over its neighbors of  $N_p$ , the third term is a bond energy contribution of a total number of bonds equal to  $N_b$ , and indexes  $a$  and  $b$  represent coordinates  $x$ ,  $y$ , and  $z$ .

The hydrostatic (mean) stress  $\sigma_h$  and in-plane stress  $\sigma_i$  can then be expressed as

$$\sigma_h = \frac{(S_{xx} + S_{yy} + S_{zz})}{3V} \quad (8)$$

$$\sigma_i = \frac{(S_{xx} + S_{yy})}{2V} \quad (9)$$

with positive and negative values denoting tensile and compressive stresses, respectively, and  $V$  representing the volume of a given domain (a slice in the present analysis).

## B. Model of the film deposition process

Carbon film formation was simulated by a single-atom deposition process. Carbon atoms were generated randomly at an  $x$ - $y$  plane above the substrate surface at a distance of 55 Å from the fixed bottom surface of the diamond substrate. To simulate the normal incidence at the diamond surface, each carbon atom was assigned a velocity in the negative  $z$ -direction and magnitude commensurate to certain energy, typical of FCVA film deposition process. In all MD simulations, the time step was set at 0.5 fs. Figure 1 shows the MD model used to simulate film formation by a single-atom deposition method. The bottom three planes of atoms of the diamond (100) substrate were fixed to mimic a semi-infinite half-

space. Atoms in the next four planes on top of the fixed atoms were assigned to an external heat bath via a Berendsen thermostat.<sup>39</sup> To minimize the effect of the thermostat on the deposition process, the remaining carbon atoms were divided into two groups. For each carbon atom generated in the simulation, all substrate atoms within a cylinder surrounding the arriving carbon atom were allowed to move freely, whereas all other remaining substrate atoms were connected to the thermostat. With this technique, atoms connected to the heat bath were updated during the deposition of each atom, and the effect of the thermostat on the interaction between deposited carbon atoms and substrate atoms was significantly reduced.

Between the deposition of two carbon atoms, the system was allowed to relax for 2 ps and then to be equilibrated by the heat bath. The relaxation time was chosen according to a study<sup>40</sup> showing a thermal spike lifetime less than 0.5 ps for ion energy less than 100 eV. Atoms sputtered off from the substrate were removed from the system before injecting a new carbon atom.

### C. Substrate model

Figure 1 shows the diamond substrate used in the present study with coordinates  $x[011]$ ,  $y[0\bar{1}1]$ , and  $z[100]$ . Periodic boundary conditions were applied to the  $x$ - and  $y$ -directions. The diamond surface in the  $z$ -direction was not constrained to allow for film growth. In each simulation, the model was first relaxed to minimize its energy such that the difference in total energy between two consecutive time steps is less than  $10^{-10}$  eV. The dimensions of the relaxed structure are  $20.17 \times 20.17 \times 60$  Å. The original substrate surface is used as the reference plane ( $z = 0$ ), while film growth occurs in the positive  $z$ -direction. Without relaxation, an internal stress was produced in the diamond substrate due to the surface tension effect of the free surface [Fig. 2(a)]. To reduce the internal stress, the diamond substrate was subjected to thermal relaxation by increasing the temperature from 300 to 800 K, keeping it at 800 K for 5 ps, decreasing it to 330 K, and finally allowing the system to relax for 5 ps. This thermal relaxation process reduced the internal stress [Fig. 2(b)], while the resulting atomic rearrangement at the diamond surface yielded 95%  $sp^2$  instead of 100%  $sp^1$  of the initial diamond surface.

## D. Ring size statistical analysis

Ring statistics was performed with the interactive structure analysis of amorphous and crystalline systems (ISAACS) program.<sup>41</sup> Rings of sizes up to 40 were analyzed with the ISAACS program.

## III. RESULTS AND DISCUSSION

### A. Film structure

Figure 3 shows *a*-C film configurations for different deposition energies. Low-energy (i.e., 1 eV) deposition produced a porous film structure dominated by  $sp^2$  hybridization without damaging the diamond substrate [Fig. 3(a)]. The formation of this film structure is attributed to the dominance of surface adsorption. The increase of  $E_d$  resulted in significantly denser film structures dominated by  $sp^3$  hybridization and the formation of an intermixing layer of progressively increased thickness [Figs. 3(b)–3(c)].

Figures 4(a)–4(d) show the initial stage of *a*-C film growth for  $E_d = 1$  eV. Impinging carbon atoms first attach to surface atoms (adsorption) and as soon as these surface sites are saturated [Fig. 4(a)] they begin to form chain-like structures of an average bond length equal to  $1.3322 \pm 0.0115$  Å [Fig. 4(b)], which is close to the double-bond length of ethylene (1.339 Å). Because this double bond is reactive, it tends to capture other carbon atoms to form a more stable single bond. Thus, deposition of more carbon atoms does not increase the chain length but causes the formation of ring-like structures [Figs. 4(c) and 4(d)]. The average bond length between  $sp^1$  and  $sp^2$  sites increases from  $1.3322 \pm 0.0115$  Å to  $1.3778 \pm 0.0129$  Å. Because of their low energy, impinging carbon atoms cannot break existing carbon bonds to penetrate into the substrate and the resulting *a*-C film structure is dominated by  $sp^2$  and  $sp^1$  hybridizations. Increasing  $E_d$  above 20 eV resulted in the formation of significantly denser films without any voids. Figures 4(e)–4(h) show the initial stage of *a*-C film growth for relatively high  $E_d = 80$  eV. Unlike the porous film structure produced with low-energy atoms, high-deposition energy significantly not only enhanced the film density but also greatly increased the  $sp^3$  content of the film. However,  $sp^2$  and  $sp^1$  hybridizations remained as the dominant types of carbon bonding at the surface. This finding suggests

that the formation of  $sp^3$  structures is mainly a consequence of the implantation mechanism that dominates the subplantation process. A comparison of simulation results for  $E_d$  in the range of 20–120 eV showed that the film surface roughness increased with  $E_d$ . This roughening effect observed at high deposition energies can be attributed to sputtering of the film by the highly energetic carbon atoms.

## **B. Film density and atom coordination**

Two important film properties are examined in this section – film density and atom coordination. Atom coordination is calculated as the number of neighboring atoms within a distance of 1.85 Å from the reference atom. The coordination number is an important parameter characterizing the composition of the *a*-C film. Atoms with a coordination number of 4 are usually referred to as tetrahedrally ( $sp^3$ ) hybridized (diamond-like), whereas atoms with a coordination number of 3 are referred to as trigonically ( $sp^2$ ) hybridized (graphite-like). Because the deposited films are not uniform in the  $z$ -direction, the properties as a function of  $z$  are calculated as averages of 0.85-Å-thick slices, which is the distance between two layers of atoms in the diamond [100] direction.

Figure 5 shows the relative density (i.e., the film density normalized by the density of the diamond substrate) and the carbon coordination fraction versus deposition energy  $E_d$ . The  $sp^3$  content sharply increases with the increase of  $E_d$  in the range of 1–20 eV and less significantly in the range of 20–80 eV, respectively. In the 20–80 eV energy range, the energetic carbon atoms can penetrate the film surface and become adsorbed in the bulk of the forming carbon film. This mechanism is known as subplantation and usually results in  $sp^3$  hybridization. In the 80–120 eV energy range, the  $sp^3$  content decreases with the increase of  $E_d$  because carbon atom rebounding onto the carbon film decreases  $sp^3$  hybridization in the bulk of the carbon film. Thus, the optimum energy for obtaining the highest  $sp^3$  content in the *a*-C film is ~80 eV, which is in agreement with experimental observations.<sup>11-14</sup> The variation of the  $sp^3$  fraction with  $E_d$  is similar to that of the film density, suggesting that denser *a*-C films are also characterized by a higher  $sp^3$  fraction.

Considering that the bond length in  $sp^3$  hybridization is longer than that in  $sp^2$  hybridization,  $a$ -C films with higher  $sp^3$  hybridization should also exhibit longer average bond length. Figure 6 shows the effect of the deposition energy  $E_d$  on the radial distribution function  $\Psi_r$ . The first peak (corresponding to the average bond length) slightly shifts to the right with the increase of  $E_d$  from 1 eV [Fig. 6(a)] to 80 eV [Fig. 6(b)], revealing an increase in the average bond length, which is consistent with the increase of  $sp^3$  hybridization. However, the first peak shifts to the left with the further increase of  $E_d$  from 80 eV [Fig. 6(c)] to 120 eV [Fig. 6(d)], implying a decrease in average bond length and, in turn,  $sp^3$  hybridization.

Changes in  $sp^3$  hybridization due to the variation of  $E_d$  are also due to the variation of the bond angle distribution in the  $a$ -C film. For purely  $sp^3$  hybridization (e.g., diamond), the bond angle is  $\sim 109^\circ$ , whereas for  $sp^2$  hybridization (e.g., graphite) it is equal to  $120^\circ$ . Thus, higher  $sp^3$  hybridization implies smaller bond angle. Figure 7 shows the dependence of the bond angle distribution  $\Phi_b$  on the deposition energy  $E_d$ . The left shift of  $\Phi_b$  with the increase of  $E_d$  from 1 eV [Fig. 7(a)] to 80 eV [Fig. 7(c)] indicates a decrease of  $sp^2$  hybridization and the simultaneous increase of  $sp^3$  hybridization. However, the further increase of  $E_d$  to 120 eV [Fig. 7(d)] leads to a right shift of  $\Phi_b$ , implying an increase in  $sp^2$  hybridization and a decrease in  $sp^3$  hybridization. Different from other  $\Phi_b$  other distributions,  $\Phi_b$  for  $E_d = 1$  eV contains a small peak at  $\sim 60^\circ$  and a significant fraction of bond angles in the range of  $140^\circ$ – $180^\circ$ , presumably due to the high fraction of  $sp^1$  hybridization in the film synthesized under deposition conditions of  $E_d = 1$  eV. With the increase of  $E_d$  above 20 eV, the fraction of  $sp^1$  hybridization decreases to almost zero. The high  $sp^1$  hybridization in the film deposited under  $E_d = 1$  eV also affects the  $\Psi_r$  distribution (Fig. 6), i.e., all  $\Psi_r$  distributions contain a small peak at 2 nm except the distribution for  $E_d = 1$  eV.

Figure 8 shows the effect of  $E_d$  on the depth distribution of the relative density and carbon atom hybridization of  $a$ -C films. The film density is normalized to that of diamond. Both low- and high-energy deposition cases reveal the existence of a three-layer structure consisting of film/substrate intermixing layer, bulk film, and surface layer. The intermixing layer consists of deposited carbon atoms and atoms of the diamond substrate. The thickness of the intermixing layer is defined as the distance from the original

surface of the diamond substrate to the location where the relative density is equal to 0.9. The intermixing layer may be interpreted as the surface layer of the diamond substrate that is damaged by the bombarding carbon atoms.<sup>16</sup> The bulk of the film is the region of nearly constant density and atom hybridization, whereas the film surface is defined as the region where the density and/or  $sp^3$  fraction sharply decrease. Low-energy deposition produces relatively thicker  $a$ -C films with negligible intermixing with the substrate and dominated by  $sp^1$  and  $sp^2$  hybridization, whereas high-energy deposition produces thinner  $a$ -C films integrated with the substrate via an intermixing layer and with much higher  $sp^3$  content.

Table I shows the effect of  $E_d$  on the thickness and density of the intermixing layer, bulk film, and surface layer. All cases show the formation of a three-layer film structure. For low-energy (1 eV) deposition, the impinging carbon atoms do not damage the diamond substrate and the thickness of the intermixing layer is negligibly small. The increase of  $E_d$  enhances the penetration of the diamond surface by carbon atoms, resulting in the formation of a thicker intermixing layer. For  $E_d = 80$  eV, the intermixing layer thickness is estimated to be 5.35 Å, which is larger than one lattice distance in the  $z$ -direction. The increase of the intermixing layer thickness with  $E_d$  suggests that more energetic atoms cause more damage to the substrate. Conversely to the intermixing layer, the bulk film thickness decreases with the increase of  $E_d$  because highly energetic atom bombardment leads to significant carbon atom implantation. The enhancement of the bombarding intensity of carbon atoms induced by the increase of  $E_d$  also has a profound effect on the bulk film density; however, the effect on the surface layer is marginal, evidently due to the significantly less bombarding carbon atoms. For relatively low  $E_d$  ( $< 20$  eV), the mobility of incident carbon atoms is limited, resulting in a thick surface layer, whereas for intermediate  $E_d$  (i.e., 20–80 eV), carbon atoms are more energetic and, therefore, can diffuse to minimum-energy sites, producing a thinner and smoother surface layer. However, at relatively high deposition energies (i.e., 120 eV), carbon atom deposition significantly exceeds atom diffusion, leading to the formation of a thicker and rougher surface layer. Among the simulation cases listed in Table I, the film with the highest bulk density (3.3 g/cm<sup>3</sup>) corresponds to  $E_d = 80$  eV. This is in agreement with experimental results showing that high-density  $a$ -C films can be obtained for  $E_d$  in the range of 80–100 eV.<sup>1</sup>

### C. Film stress

Figure 9 shows the variation of the hydrostatic stress  $\sigma_h$  [Eq. (8)] and the in-plane stresses  $\sigma_i$  [Eq. (9)] with the deposition energy  $E_d$ . The hydrostatic stress is the average of all the stresses parallel and perpendicular to the film surface. Because stresses parallel to the film surface are much higher than the out-of-plane stress,  $\sigma_h$  is always less than  $\sigma_i$ . While low-energy (1 eV) deposition produces a mild tensile stress, increasing  $E_d$  leads to the development of high compressive stresses in the film. This trend is in agreement with the increase of the  $sp^3$  fraction (Fig. 5) and bulk film density (Table I) with  $E_d$ .

Figure 10 shows through-thickness distributions of hydrostatic and in-plane stress for  $E_d = 1$  and 80 eV. Low-energy deposition produces relatively low and mainly tensile film stress [Fig. 10(a)], attributed to the stretching effect of excess  $sp^1$  dangling bonds at the surface, which are less constrained because they have fewer neighboring atoms. Because a tensile stress is not conducive to  $sp^3$  hybridization, the  $sp^3$  fraction in the film synthesized under low-energy (1 eV) deposition conditions is less than 5% [Figs. 5 and 8(a)]. However, relatively high-energy (80 eV) deposition produces a compressive film stress between  $-17$  and  $-22$  GPa, which is in fair agreement with experimentally measured compressive stresses varying between  $-11$  and  $-15$  GPa.<sup>11,42-43</sup> The discrepancy between MD results and experimental measurements may be due to the periodic boundary condition applied to the  $x$ - and  $y$ -directions and errors introduced in the experimental measurements of the film stress (e.g., errors in the measurement of the very sample curvature induced by the stress in very thin films). In both simulation cases, both  $\sigma_h$  and  $\sigma_i$  decrease close to zero at the surface, providing validation to the method used to calculate the film stresses (section IIB).

### D. Intermediate-range order and ring size statistics

Intermediate-range order refers to the order of the atomic structure at length scales larger than one or two times the average bond length and correlates to the mechanical, optical, and electric properties of amorphous materials.<sup>30,31</sup> The most widely used approach for studying intermediate-range order, especially in numerical simulations, is the ring size statistics originated from graph theory.<sup>44-46</sup> A ring is

defined as a closed loop consisting of atoms connected to each other by bonds. The ring size is defined as the number of atoms in the ring. To calculate the number of rings and the connectivity of the rings, it is necessary to identify first those rings that are relevant to intermediate-range order. Primitive rings (i.e., rings that cannot be divided into smaller rings), which are closely related to intermediate-range order, are considered in the present study.<sup>47–48</sup> Carbon atoms within a distance range in the  $z$ -direction of 15–30 Å are considered in the present ring statistics. Since the initial thickness of the diamond substrate is equal to ~14 Å, atoms within a depth distance of 15–30 Å provide a good representation of the atomic structure of the  $a$ -C film.

Figure 11 shows the ring size distribution  $\Phi_r$  (defined as the ratio of the number of rings to the total number of atoms in the system) as a function of ring size  $d$  (expressed in number of atoms) for  $E_d = 1–120$  eV. The cut-off ring size is equal to 3 because the smallest ring contains three atoms. Low-energy deposition produces a wide  $\Phi_r$  distribution in the range  $3 < d < 40$  [Fig. 11(a)]; however, the increase of  $E_d$  to 20 eV yields a tighter  $\Phi_r$  distribution in the range  $3 < d < 16$  and the average  $d$  is equal to ~8 [Fig. 11(b)], indicating a carbon atom network of increased order. Even tighter  $\Phi_r$  distribution is shown for  $E_d = 80$  eV and average  $d$  decreases to 6 [Fig. 11(c)]. Thus, a further order increase of the atomic network is encountered in the intermediate range of  $E_d$ . Because both diamond (pure  $sp^3$  hybridization) and graphite (pure  $sp^2$  hybridization) have  $d = 6$ , the shift of  $\Phi_r$  to the left may be interpreted as an increase of both  $sp^2$  and  $sp^3$  hybridizations. The increase of  $E_d$  from 80 to 120 eV leads to a decrease in intermediate-range order, as evidenced by the wider  $\Phi_r$  distribution and the increase of average  $d$  to 7 [Fig. 11(d)].

Figure 12 shows the atom distribution  $\Phi_a$  (defined as the number of atoms contributing to the formation of rings of a given size divided by the total number of atoms in the system) as a function of ring size  $d$  for  $E_d = 1–120$  eV. Atoms shared by two or more rings of the same size are only counted once. The wide  $\Phi_a$  distribution obtained for  $E_d = 1$  eV [Fig. 12(a)] is consistent with that shown in Fig. 11(a). For  $E_d = 20$  and 80 eV [Fig. 12(b) and 12(c), respectively],  $\Phi_a$  is centered in the range  $6 < d < 9$ , whereas for  $E_d = 120$  eV [Fig. 12(d)],  $\Phi_a$  is wider than the distributions obtained for  $E_d = 20$  and 80 eV. The effect of  $E_d$

on the number of atoms shared by rings of a given size may be interpreted in the context of the results shown in Figs. 11 and 12. If rings of a given size do not share any atoms, the atoms involved in the formation of these rings will be equal to the ring size times the number of rings, and high  $\Phi_r$  will result in high  $\Phi_a$ . Consequently, high  $\Phi_r$  and low  $\Phi_a$  implies significant atom sharing among rings of a given size (i.e., high ring connectivity). A comparison of Figs. 11(b) and 11 (c) shows that  $\Phi_r(d = 6, E_d = 20 \text{ eV})$  is smaller than  $\Phi_r(d = 6, E_d = 80 \text{ eV})$  whereas a comparison of Figs. 12(b), 12(c) shows that  $\Phi_a(d = 6, E_d = 20 \text{ eV})$  is similar to  $\Phi_a(d = 6, E_d = 80 \text{ eV})$ ; implying that more rings with  $d = 6$  share atoms in the *a*-C films synthesized under 80 than 20 eV deposition energy. A similar observation can be made for  $d = 7$ . For  $E_d = 80 \text{ eV}$ ,  $\Phi_r(d = 9) > \Phi_r(d = 6 \text{ or } 7)$  [Fig. 11(b)], while  $\Phi_a(d = 6)$ ,  $\Phi_a(d = 7)$ , and  $\Phi_a(d = 9)$  are similar [Fig. 12(b)], indicating that rings with  $d = 9$  share more atoms with each other than rings with  $d = 6$  or 7.

Further insight into intermediate-range ordering can be obtained by considering the normalized atom distribution  $\Phi_a^*$ , defined as  $\Phi_a$  for a given  $d$  to the maximum value of  $\Phi_a$ , denoted by  $\Phi_{a,max}$ , calculated from the ring size distribution  $\Phi_r$  (Fig. 11). Assuming that there are no rings of a given size  $d$  sharing  $n$  atoms,  $\Phi_{a,max} = n\Phi_r(d)$ . Figure 13 shows the normalized atom distribution  $\Phi_a^*$  as a function of ring size  $d$ .  $\Phi_a^* = 1$  implies no atom sharing among rings of the same size, whereas low  $\Phi_a^*$  values indicate the existence of a significant number of atoms that are shared among rings of the same size. For  $E_d = 1 \text{ eV}$ , atom sharing is insignificant for almost all rings of a given size [Fig. 13(a)], while for  $E_d = 20 \text{ eV}$ , atom sharing is mainly observed for rings with sizes in the range  $5 < d < 14$  [Fig. 13(b)]. More atom sharing among rings of a given size is observed with the increase of  $E_d$  to 80 eV [Fig. 13(c)]; however, the overall  $\Phi_a^*$  distribution is similar to that for  $E_d = 20 \text{ eV}$ . Atom sharing among rings with sizes in the range  $5 < d < 10$ , where the majority of rings exist for  $E_d = 20, 80, \text{ and } 120 \text{ eV}$  (Fig. 11), is similar for  $E_d = 20$  and 80 and less for  $E_d = 120 \text{ eV}$  [Fig. 13(d)].

Further insight into intermediate-range atom ordering can be obtained by considering the normalized maximum and minimum atom distributions  $\Phi_{a,max}^*$  and  $\Phi_{a,min}^*$ , representing the fractions of

atoms contributing to the formation of rings of a given size, which are also present in the rings that have the given size as maximum or minimum. For example, if  $n$  atoms contribute to the formation of all rings of a given size  $d^*$ , some of these atoms may also contribute to the formation of rings of other sizes. If  $k$  and  $m$  atoms among the  $n$  atoms are also present in rings that have  $d^*$  as maximum and minimum size, respectively, then  $\Phi_{a,max}^* = k/n$  and  $\Phi_{a,min}^* = m/n$ . Figure 14 shows the effect of the deposition energy  $E_d$  on  $\Phi_{a,max}^*$  and  $\Phi_{a,min}^*$ . High  $\Phi_{a,max}^*$  implies less atoms of rings of a given size shared with larger rings, whereas high  $\Phi_{a,min}^*$  implies less atoms of rings of a given size shared with smaller rings. For  $E_d = 1$  eV,  $\Phi_{a,max}^*$  assumes low values in the range  $3 < d < 8$  [Fig. 14(a)], indicating a high connectivity among rings with  $d > 8$ , whereas  $\Phi_{a,min}^*$  assumes high values in the same range [Fig. 14(e)], indicating a low connectivity among rings with  $3 \leq d \leq 8$ . In addition, the decreasing trend of  $\Phi_{a,min}^*$  for  $d > 10$  implies a sharply increasing connectivity among rings with  $d > 10$  and  $3 \leq d \leq 10$ . For  $E_d = 20$  and 80 eV,  $\Phi_{a,max}^*$  obtains higher values in the relatively large-ring range  $13 \leq d \leq 16$  [Figs. 14(b) and 14(c)], whereas  $\Phi_{a,min}^*$  assumes relatively smaller values in the small-ring range  $3 \leq d \leq 10$  [Figs. 14(f) and 14(g)], implying weak and strong connectivity for relatively large and small rings, respectively. Also, the very low  $\Phi_{a,max}^*$  values and very high  $\Phi_{a,min}^*$  values in the range  $3 \leq d \leq 6$  indicate a strong connectivity between small and large rings in the  $a$ -C films deposited for  $E_d = 20$  and 80 eV. Although  $\Phi_{a,max}^*$  and  $\Phi_{a,min}^*$  for  $E_d = 20$  and 80 eV are similar, a comparison of Figs. 14(b), 14(c), 14(f), and 14(g) indicates slightly stronger connectivity of small rings for  $E_d = 80$  eV than 20 eV. Compared to the rings corresponding to  $E_d = 1$  eV, both 20 and 80 eV have tighter ring size distributions and stronger connectivity among small rings and among small and large rings are obtained for  $E_d = 20$  and 80 eV compared to 1 eV. Considering that the majority of the rings for  $E_d = 20$  and 80 eV [Figs. 12(b) and 12(c)] are smaller than those for  $E_d = 1$  eV [Fig. 12(a)], it may be inferred that connectivity was significantly enhanced by the increase of the deposition energy. Although the connectivity of small rings ( $3 \leq d \leq 6$ ) for  $E_d = 120$  eV [Figs. 14(d) and 14(h)] is only slightly worse than those for  $E_d = 80$  eV [Figs. 14(c) and 14(g)], the  $a$ -C film contains large

rings ( $d > 16$ ) connected to small and large rings; however, connectivity for  $E_d = 120$  eV is better than that for  $E_d = 1$  eV, as indicated by the small range of  $\Phi_{a,min}^*$  [Fig. 14(h)].

#### IV. CONCLUSIONS

The structure, properties, and internal stress of ultrathin *a*-C films synthesized by energetic atoms were examined in the context of MD simulation results. Atom-atom interaction was described by the second-generation REBO potential. All simulations revealed the formation of three-layer structure consisting of intermixing layer, bulk film, and surface layer. The film structure (atom hybridization), density, and residual stress showed a strong dependence on the energy of impinging carbon atoms (deposition energy  $E_d$ ). Film density, residual stress, and  $sp^3$  content increased with  $E_d$ , in agreement with experimental results. Relatively high  $E_d$  (e.g., 120 eV) caused damage to the substrate surface and led to the formation of a thicker surface layer dominated by  $sp^2$  and  $sp^1$  hybridizations and surface dangling bonds. For the range of  $E_d$  examined (1–120 eV), optimum film properties, i.e., maximum density, thinnest intermixing and surface layers, and highest  $sp^3$  fraction, were obtained for  $E_d = 80$  eV, also in agreement with experimental findings.

Atom collision during deposition led to the development of an internal stress in the film. Low-energy ( $E_d = 1$  eV) deposition produced a tensile film stress, in agreement with the dominant presence of  $sp^1$  and  $sp^2$  hybridizations at the film surface, which are reactive and tend to induce stretching of the film. High-energy ( $E_d > 20$  eV) deposition resulted in a compressive state in the films, with a hydrostatic stress between  $-11$  and  $-13$  GPa. Because a local compressive environment is conducive to  $sp^3$  hybridization and the compressive stress in the film increased with  $E_d$ , *a*-C films with high  $sp^3$  content were produced with highly energetic carbon atoms.

The structure and properties of *a*-C films synthesized by energetic particle deposition methods, such as FCVA, strongly depend on the intensity that impinging carbon atoms interact with substrate atoms. Low-energy carbon atoms are mainly adsorbed at the surface of the growing film, resulting in  $sp^2$  and  $sp^1$  hybridization. However, high-energy carbon atoms penetrate the film surface, inducing

subsurface interactions that favor  $sp^3$  hybridization. High-energy carbon atoms may also rebound from the surface or sputter off atoms adsorbed onto the surface of the growing film.

Ring-size statistics provided insight into the effect of energetic atom impingement on intermediate-range atomic ordering. Low-energy ( $E_d = 1$  eV) deposition produced  $a$ -C films with the widest ring size distribution and lowest ring connectivity. Increasing  $E_d$  to 20 and 80 eV resulted in tighter ring size distributions and increased ring connectivity. However, a further increase of  $E_d$  to 120 eV resulted in broader ring size distribution and decreased connectivity of small rings.

The MD results of this study are in good qualitative agreement with experimental results of the optimum deposition energy and internal stress of  $a$ -C films deposited by energetic particle deposition methods. The findings of this investigation are also complementary to experimental studies because they provide insight into the formation of a three-layer film structure, the evolution of damage at the substrate surface, and the intermediate-range order for different deposition energies, which is cumbersome to identify by experimental methods.

## Acknowledgement

This research was funded by the Computer Mechanics Laboratory (CML) and the UCB-KAUST Academic Excellence Alliance (AEA) Program.

## References

- [1] J. Robertson: Diamond-like amorphous carbon. *Mater. Sci. Eng. R* **37**, 129–281 (2002).
- [2] M.K. Fung, K.H. Lai, C.Y. Chan, I. Bello, C.S. Lee, S.T. Lee, D.S. Mao, and X. Wang: Mechanical properties and corrosion studies of amorphous carbon on magnetic disks prepared by ECR plasma technique. *Thin Solid Films* **368**, 198–202 (2000).
- [3] R. Hauert: An overview on the tribological behavior of diamond-like carbon in technical and medical applications. *Tribol. Int.* **37**, 991–1003 (2004).
- [4] A. Erdemir and C. Donnet: Tribology of diamond-like carbon films: recent progress and future prospects. *J. Phys. D: Appl. Phys.* **39**, R311–R327 (2006).

- [5] I.G. Brown: Cathodic arc deposition of films. *Annu. Rev. Mater. Sci.* **28**, 243–269 (1998).
- [6] A.A. Voevodin and M.S. Donley: Preparation of amorphous diamond-like carbon by pulsed laser deposition: a critical review. *Surf. Coat. Technol.* **82**, 199–213 (1996).
- [7] H.-S. Zhang and K. Komvopoulos: Direct-current cathodic vacuum arc system with magnetic-field mechanism for plasma stabilization. *Rev. Sci. Instrum.* **79**, 073905 (2008).
- [8] N. Wang and K. Komvopoulos: Incidence angle effect of energetic carbon ions on deposition rate, topography, and structure of ultrathin amorphous carbon films deposited by filtered cathodic vacuum arc. *IEEE Trans. Magn.* **48**, 2220–2227 (2012).
- [9] A. Anders, W. Fong, A. V. Kulkarni, F. W. Ryan, and C. S. Bhatia: Ultrathin diamond-like carbon films deposited by filtered carbon vacuum arcs. *IEEE T. Plasma Sci.* **29**, 768–775 (2001).
- [10] A. Anders: Energetic deposition using filtered cathodic arc plasmas. *Vacuum* **67**, 673–686 (2002).
- [11] P. J. Fallon, V. S. Veerasamy, C. A. Davis, J. Robertson, G. A. J. Amaratunga, W. I. Milne, and J. Koskinen: Properties of filtered-ion-beam deposited diamondlike carbon as a function of ion energy. *Phys. Rev. B.*, **48**, 4777–4782 (1993).
- [12] G. M. Pharr, D. L. Callahan, S. D. McAdams, T. Y. Tsui, S. Anders, A. Anders, J. W. Ager III, I. G. Brown, C. S. Bhatia, S. R. P. Silva and J. Robertson: Hardness, elastic modulus, and structure of very hard carbon films produced by cathodic-arc deposition with substrate pulse biasing. *Appl. Phys. Lett.* **68**, 779–781 (1996).
- [13] M. Chhowalla, J. Robertson, C. W. Chen, S. R. P. Silva, C. A. Davis, G. A. J. Amaratunga and W. I. Milne: Influence of ion energy and substrate temperature on the optical and electronic properties of tetrahedral amorphous carbon (ta-C) films. *J. Appl. Phys.* **81**, 139–145 (1997).
- [14] E. Byon and A. Anders: Ion energy distribution functions of vacuum arc plasmas. *J. Appl. Phys.* **93**, 1899 (2003).
- [15] Y. Lifshitz, S.R. Kasi, J.W. Rabalais, and W. Eckstein: Subplantation model for film growth from hyperthermal species. *Phys. Rev. B* **41**, 10468 (1990).

- [16] N. Wang and K. Komvopoulos: The multilayered structure of ultrathin amorphous carbon films synthesized by filtered cathodic vacuum arc deposition. *J. Mater. Res.* **28**, 2124–2131 (2013).
- [17] C.A. Davis, G.A.J. Amaratunga, and K.M. Knowles: Growth mechanism and cross-sectional structure of tetrahedral amorphous carbon thin films. *Phys. Rev. Lett.* **80**, 3280–3283 (1998).
- [18] C.A. Davis, K.M. Knowles, and G.A.J. Amaratunga: Cross-sectional structure of tetrahedral amorphous carbon thin films. *Surf. Coat. Technol.* **76-77**, 316–321 (1995).
- [19] H. –P. Kaukonen and R. M. Nieminen: Molecular-dynamics simulation of the growth of diamondlike films by energetic carbon-atom beams. *Phys. Rev. Lett.* **68**, 620–623 (1992).
- [20] J. Tersoff: New empirical approach for the structure and energy of covalent systems. *Phys. Rev. B* **37**, 6991–7000 (1988).
- [21] J. Tersoff: Modeling solid-state chemistry: interatomic potentials for multicomponent systems. *Phys. Rev. B* **39**, 5566–5568 (1989).
- [22] N. A. Marks, D. R. McKenzie, and B. A. Pailthorpe: Molecular-dynamics study of compressive stress generation. *Phys. Rev. B* **53**, 4117–4124 (1996).
- [23] F. H. Stillinger and T. A. Weber: Computer simulation of local order in condensed phases of silicon. *Phys. Rev. B* **31**, 5262–5271 (1985).
- [24] H. U. Jager and K. Albe: Molecular-dynamics simulations of steady-state growth of ion-deposited tetrahedral amorphous carbon films. *J. Appl. Phys.* **88**, 1129–1135 (2000).
- [25] D. W. Brenner: Empirical potential for hydrocarbons for use in simulating the chemical vapor deposition of diamond films. *Phys. Rev. B* **42**, 9458–8471 (1990).
- [26] D. W. Brenner: Erratum: Empirical potential for hydrocarbons for use in simulating the chemical vapor deposition of diamond films. *Phys. Rev. B* **46**, 1948–1948 (1992).
- [27] D. W. Brenner, O. A. Shenderova, J. A. Harrison, S. J. Stuart, B. Ni and S. B. Sinnott: A second-generation reactive empirical bond order (REBO) potential energy expression for hydrocarbons. *J. Phys: Cond. Matter.* **14**, 783–802 (2002).

- [28] T. Ma, Y.-Z. Hu, H. Wang, and X. Li: Microstructure and stress properties of ultrathin diamondlike carbon films during growth: Molecular dynamics simulations. *Phys. Rev. B* **75**, 035425 (2007).
- [29] N. Wang and K. Komvopoulos: Thermal stability of ultrathin amorphous carbon films for energy-assisted magnetic recording. *IEEE Trans. Magn.* **47**, 2277–2282 (2011).
- [30] J. D. Martin, S. J. Goettler, N. Fosse, and L. Iton: Designing intermediate-range order in amorphous materials. *Nature* **419**, 381–384 (2002).
- [31] S. Kohara, J. Akola, H. Morita, K. Suzuya, J. K. R. Weber, M. C. Wilding, and C. J. Benmore: Relationship between topological order and glass forming ability in densely packed enstatite and forsterite composition glasses. *Proc. Nat. Acad. Sci. USA* **108**, 14780–14785 (2011).
- [32] J. P. Rino, I. Ebbsjo, P. S. Branicio, R. K. Kalia, A. Nakano, F. Shimojo, and P. Vashishta: Short- and intermediate-range structural correlations in amorphous silicon carbide: A molecular dynamics study. *Phys. Rev. B* **70**, 045207 (2004).
- [33] M. Guthrie, C. A. Tulk, C. J. Benmore, J. Xu, J. L. Yarger, D. D. Klug, J. S. Tse, H-K. Mao, and R. J. Hemley: Formation and structure of a dense octahedral glass. *Phys. Rev. Letters* **93**, 115502 (2004).
- [34] M. P. Allen and D. J. Tildesley, *Computer Simulation of Liquids* (Oxford University Press, New York, 1989).
- [35] S. J. Stuart, A. B. Tutein, and J. A. Harrison: A reactive potential for hydrocarbons with intermolecular interactions. *J. Chem. Phys.* **112**, 6472–6486 (2002).
- [36] D. Levesque and L. Verlet: Molecular dynamics and time reversibility. *J. Stat. Phys.* **72**, 519–537 (1993).
- [37] S. J. Plimpton: Fast parallel algorithms for short-range molecular dynamics. *J. Comp. Phys.* **117**, 1–9 (1995).
- [38] N. A. Marks: Thin film deposition of tetrahedral amorphous carbon: a molecular dynamics study. *Diamond Relat. Mater.* **14**, 1223–1232 (2005).

- [39] H. J. C. Berendsen, J. P. M. Postma, W. F. van Gunsteren, A. DiNola, and J. R. Haak: Molecular dynamics with coupling to an external bath. *J. Chem. Phys.* **81**, 3684–3690 (1984).
- [40] N. A. Marks: Evidence for subpicosecond thermal spikes in the formation of tetrahedral amorphous carbon. *Phys. Rev. B* **56**, 2441–2446 (1997).
- [41] S. L. Roux and P. Jund: ISAACS – Interactive structure analysis of amorphous and crystalline systems. *J. Appl. Cryst.* **43**, 181–185(2010).
- [42] M. C. Polo, J. L. Andujar, A. Hart, J. Robertson, W. I. Milne: Preparation of tetrahedral amorphous carbon films by filtered cathodic vacuum arc deposition. *Diamond Relat. Mater.* **9**, 663–667 (2000).
- [43] A. C. Ferrari, S. E. Rodil, J. Robertson, W. I. Milne: Is stress necessary to stabilize sp<sup>3</sup> bonding in diamond-like carbon?. *Diamond Relat. Mater.* **11**, 994–999 (2002).
- [44] S. V. King: Ring configuration in a random walk model of vitreous silica. *Nature* **213**, 1112 (1967).
- [45] D. S. Franzblau: Computation of ring statistics for network models of solids. *Phys. Rev. B* **44**, 4925–4929 (1991).
- [46] L. Guttman: Ring structure of the crystalline and amorphous forms of silicon dioxide. *J. Non-Cryst. Solids* **116**, 145–147(1990).
- [47] X. Yuan and A. N. Cormack: Efficient algorithm for primitive ring statistics in topological networks. *Comp. Mater. Sci.* **24**, 343-360(2002)
- [48] S. L. Roux and P. Jund: Ring statistics analysis of topological networks: New approach and application to amorphous GeS<sub>2</sub> and SiO<sub>2</sub> systems. *Comp. Mater. Sci.* **49**, 70–83(2010).

Table I. Effect of deposition energy on the thickness and density of intermixing layer, bulk film, and surface layer.

Deposition energy (eV)	Thickness (Å)			Density (g/cm <sup>3</sup> )	
	Intermixing layer	Bulk film	Surface layer	Bulk film	Surface layer
1	0.1	35	6.6	1.68	0.97
20	2.68	20.52	2.7	3.13	0.98
80	5.35	15.17	9.33	3.30	1.79
120	6.14	14.28	11.41	3.19	1.58

## List of Figures

- Fig. 1 Molecular dynamics model of film deposition by energetic atoms.
- Fig. 2 Depth profiles of hydrostatic stress  $\sigma_h$  and in-plane stress  $\sigma_i$  in the diamond substrate (a) before and (b) after thermal relaxation.
- Fig. 3 Film structure for deposition energy  $E_d$  equal to (a) 1, (b) 20, (c) 80, and (d) 120 eV. Atoms with a different coordination number are shown in different color (gray:  $sp^3$ , green:  $sp^2$ , yellow:  $sp^1$ , and blue:  $sp$ ).
- Fig. 4 Initial stage of film growth for deposition energy  $E_d$  equal to 1 eV (first row) and 80 eV (second row).
- Fig. 5 Relative film density and carbon atom hybridization versus deposition energy  $E_d$ . The film density was normalized by the density of the diamond substrate.
- Fig. 6 Radial distribution function  $\Psi_r$  for deposition energy  $E_d$  equal to (a) 1, (b) 20, (c) 80, and (d) 120 eV.
- Fig. 7 Bond angle distribution  $\Phi_b$  for deposition energy  $E_d$  equal to (a) 1, (b) 20, (c) 80, and (d) 120 eV. Bond angles of  $109^\circ$  (pure  $sp^3$  hybridization) and  $120^\circ$  (pure  $sp^2$  hybridization) corresponding to diamond and graphite, respectively, are marked by dashed lines.
- Fig. 8 Depth profiles of relative film density and carbon atom hybridization for deposition energy  $E_d$  equal to (a) 1 and (b) 80 eV. The film density was normalized by the density of the diamond substrate.
- Fig. 9 Hydrostatic stress  $\sigma_h$  and in-plane stress  $\sigma_i$  versus deposition energy  $E_d$ .
- Fig. 10 Depth profiles of hydrostatic stress  $\sigma_h$  and in-plane stress  $\sigma_i$  for deposition energy  $E_d$  equal to (a) 1 and (b) 80 eV. The vertical dashed line indicates the original substrate surface.
- Fig. 11 Ring size distribution  $\Phi_r$  for deposition energy  $E_d$  equal to (a) 1, (b) 20, (c) 80, and (d) 120 eV.
- Fig. 12 Atom distribution  $\Phi_a$  for deposition energy  $E_d$  equal to (a) 1, (b) 20, (c) 80, and (d) 120 eV.

Fig. 13 Normalized atom distribution  $\Phi_a^*$  for deposition energy  $E_d$  equal to (a) 1, (b) 20, (c) 80, and (d) 120 eV.

Fig. 14 Normalized maximum and minimum atom distributions  $\Phi_{a,max}^*$  and  $\Phi_{a,min}^*$ , respectively, for deposition energy  $E_d$  equal to (a,e) 1, (b,f) 20, (c,g) 80, and (d,h) 120 eV.

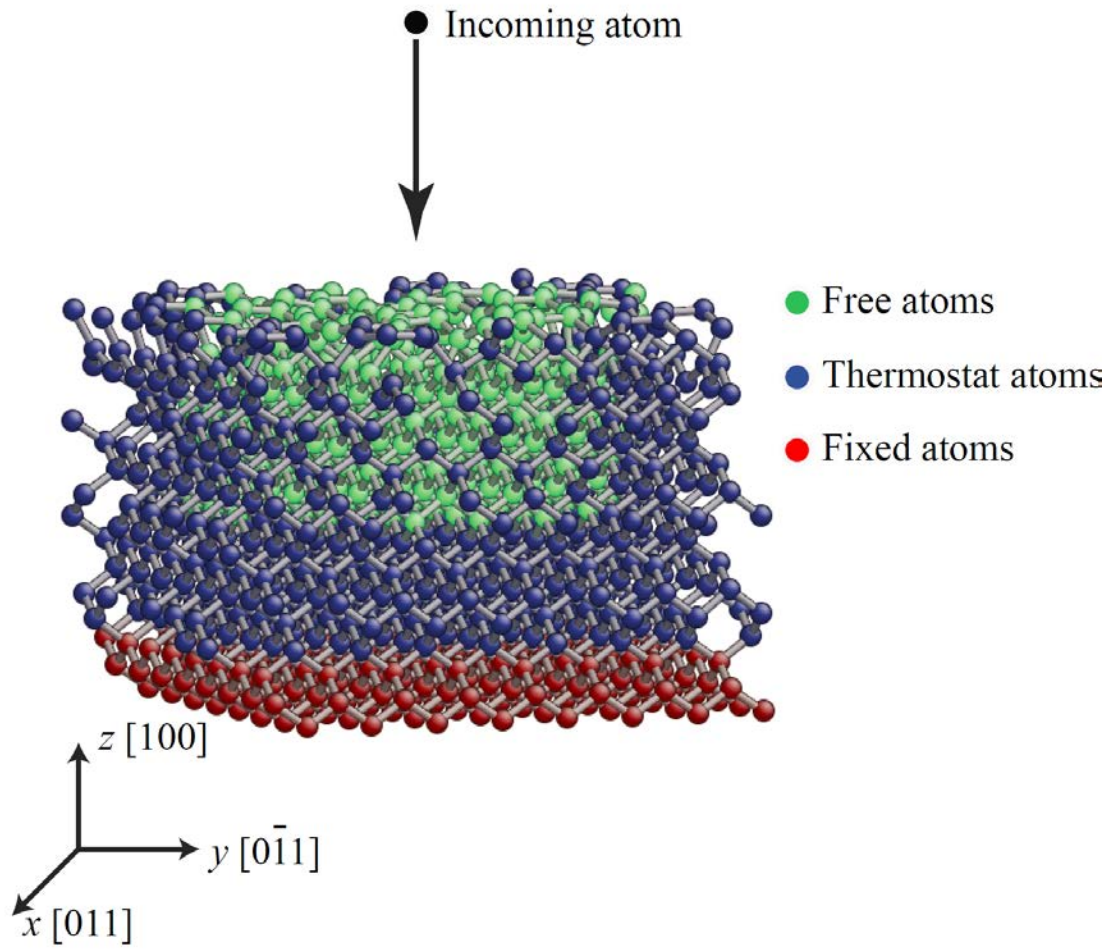


**Figure 1**

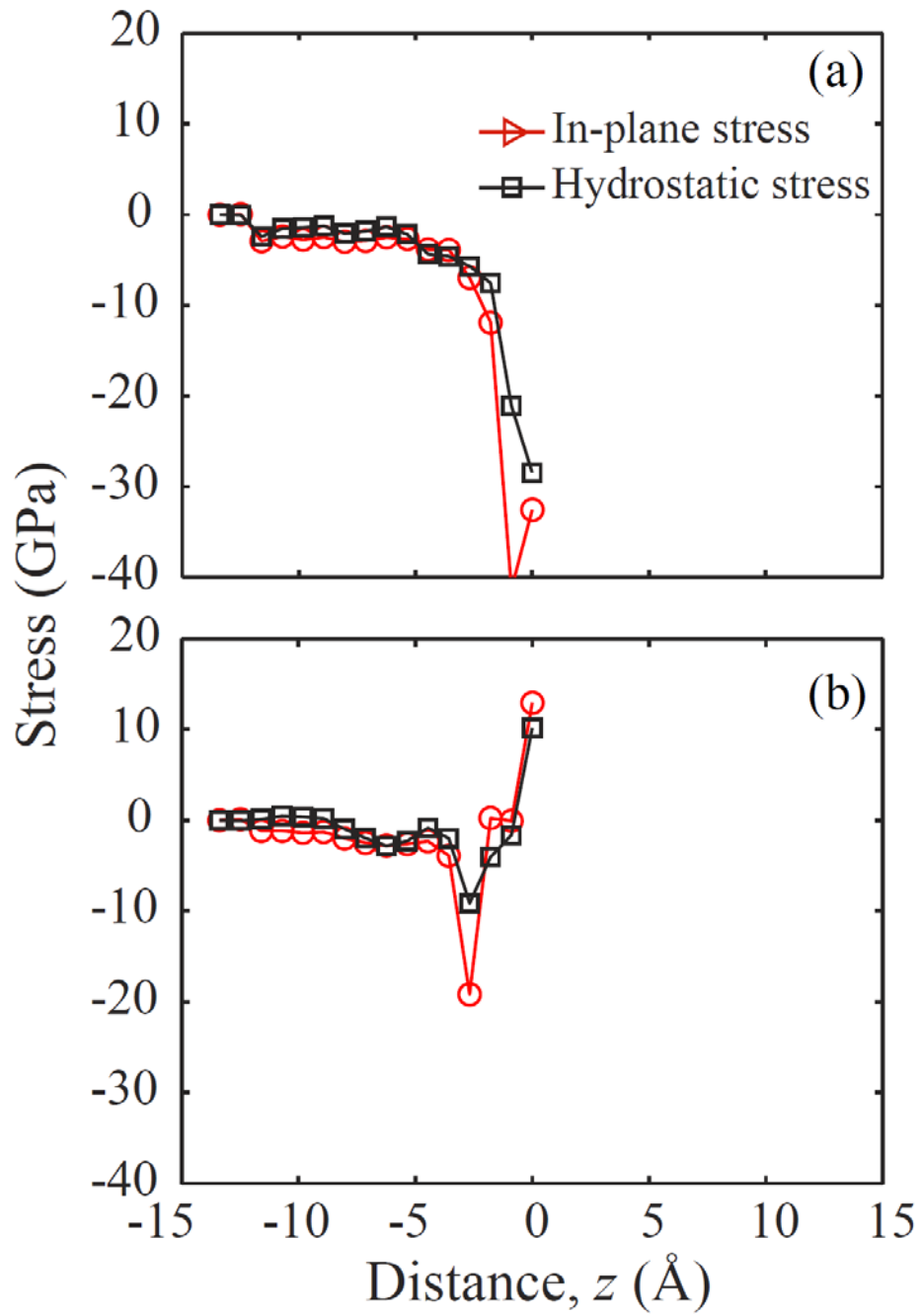
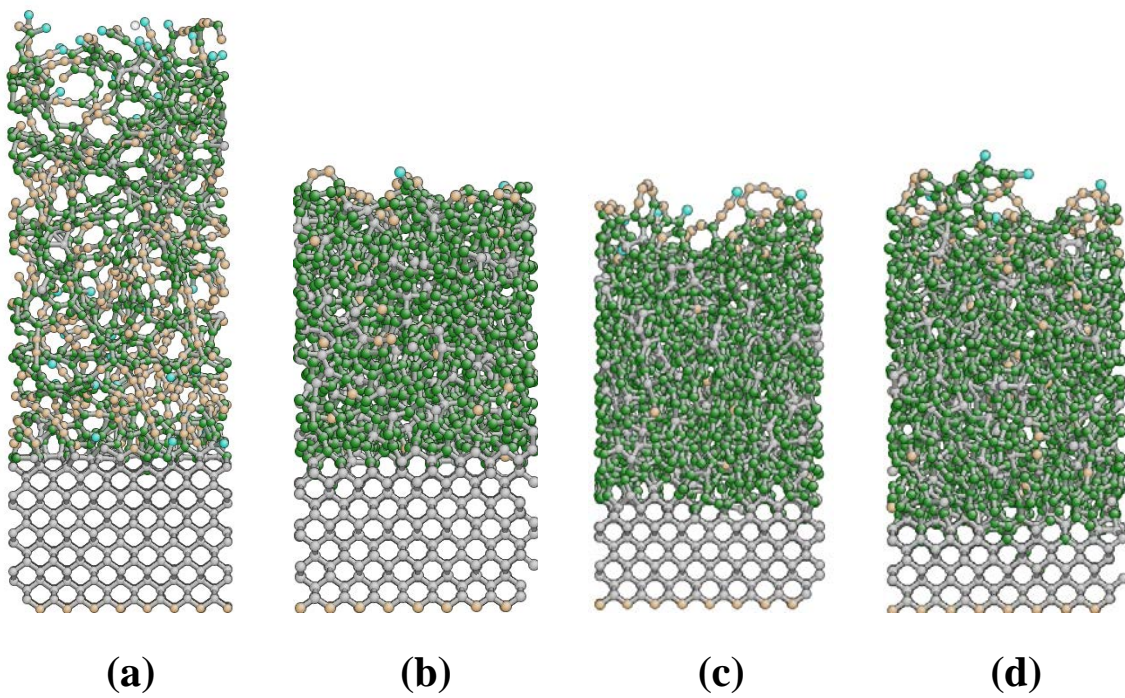
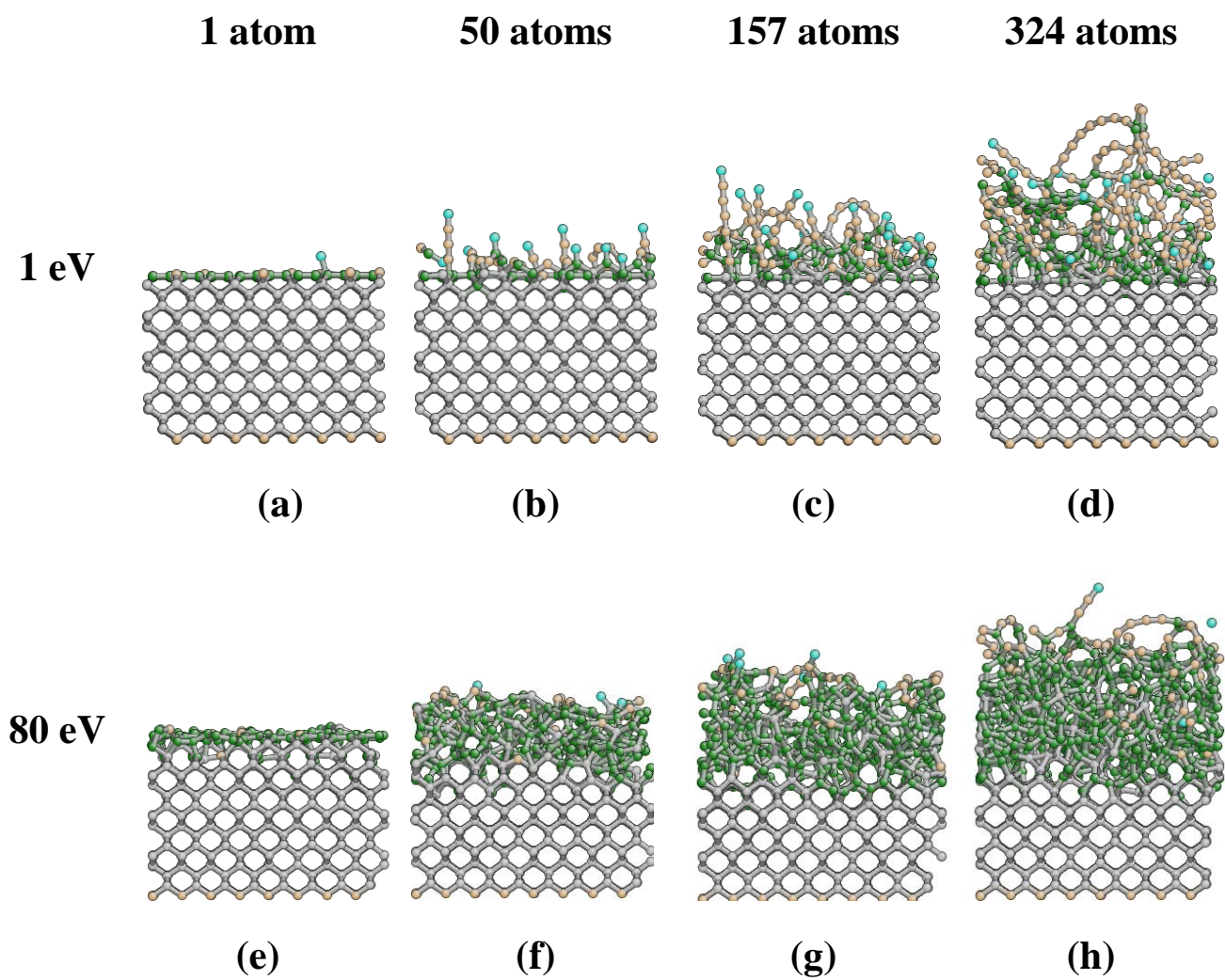


Figure 2



**Figure 3**



**Figure 4**

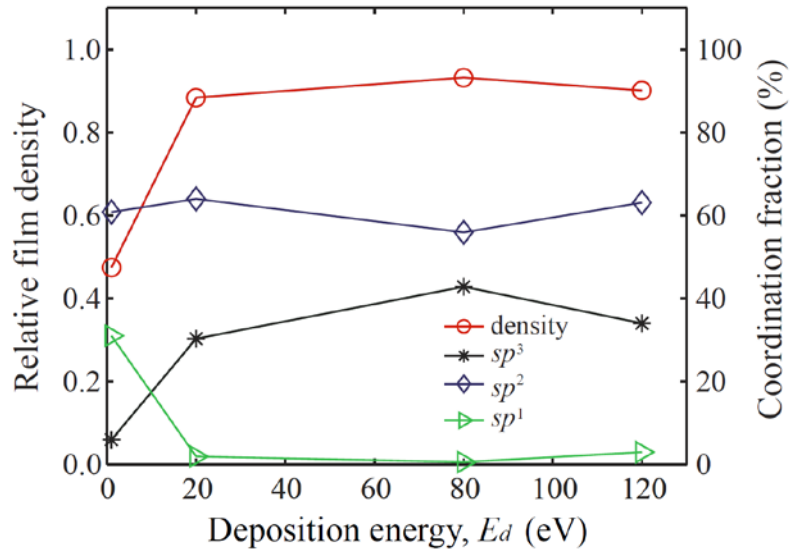


**Figure 5**

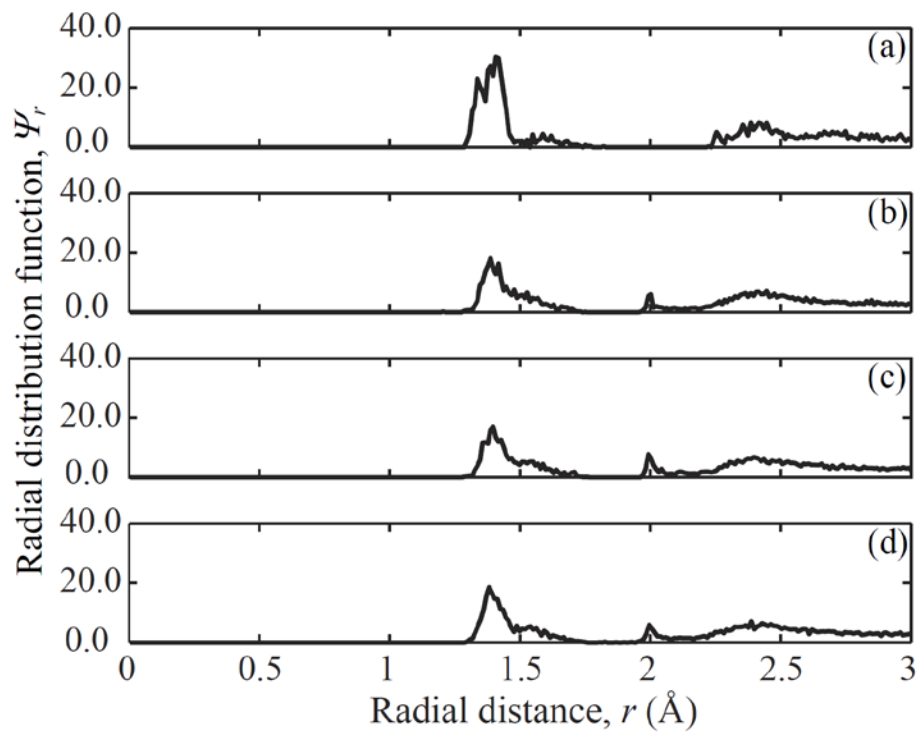


**Figure 6**

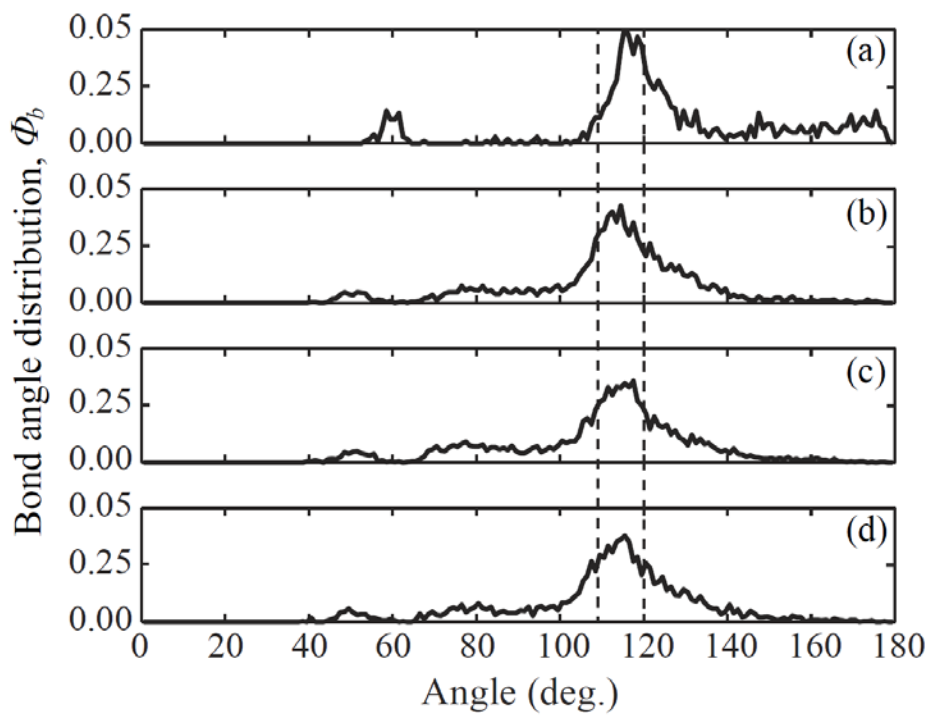


**Figure 7**

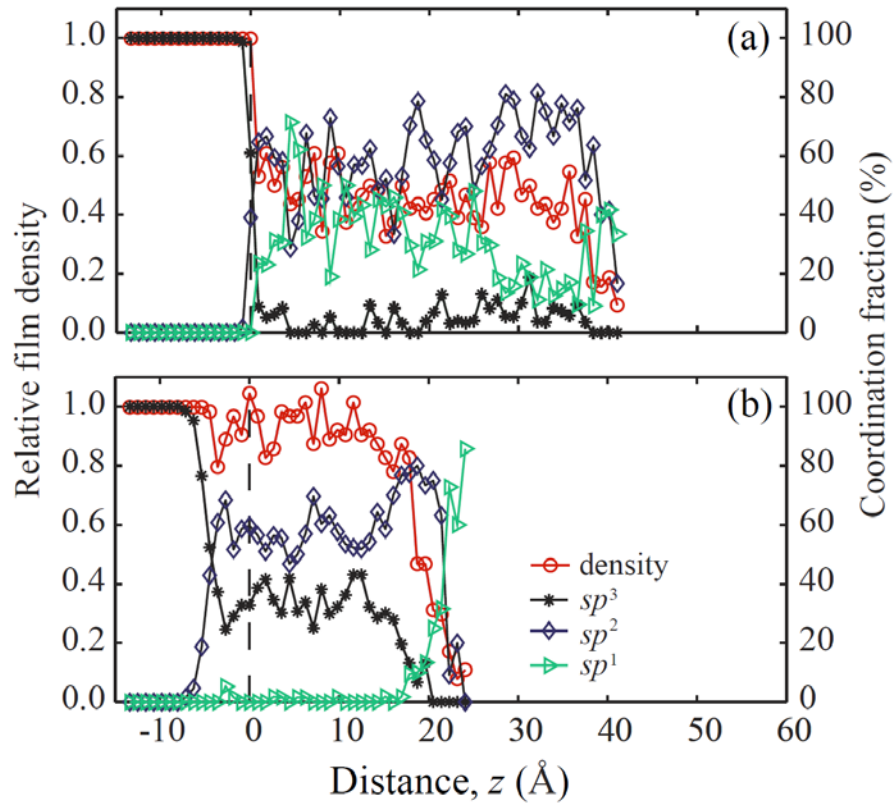


**Figure 8**

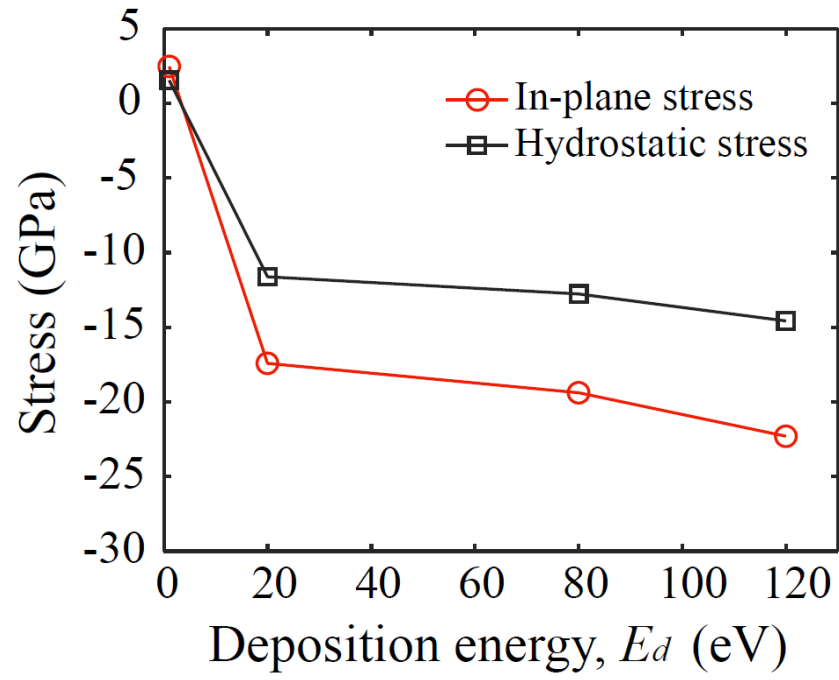


**Figure 9**

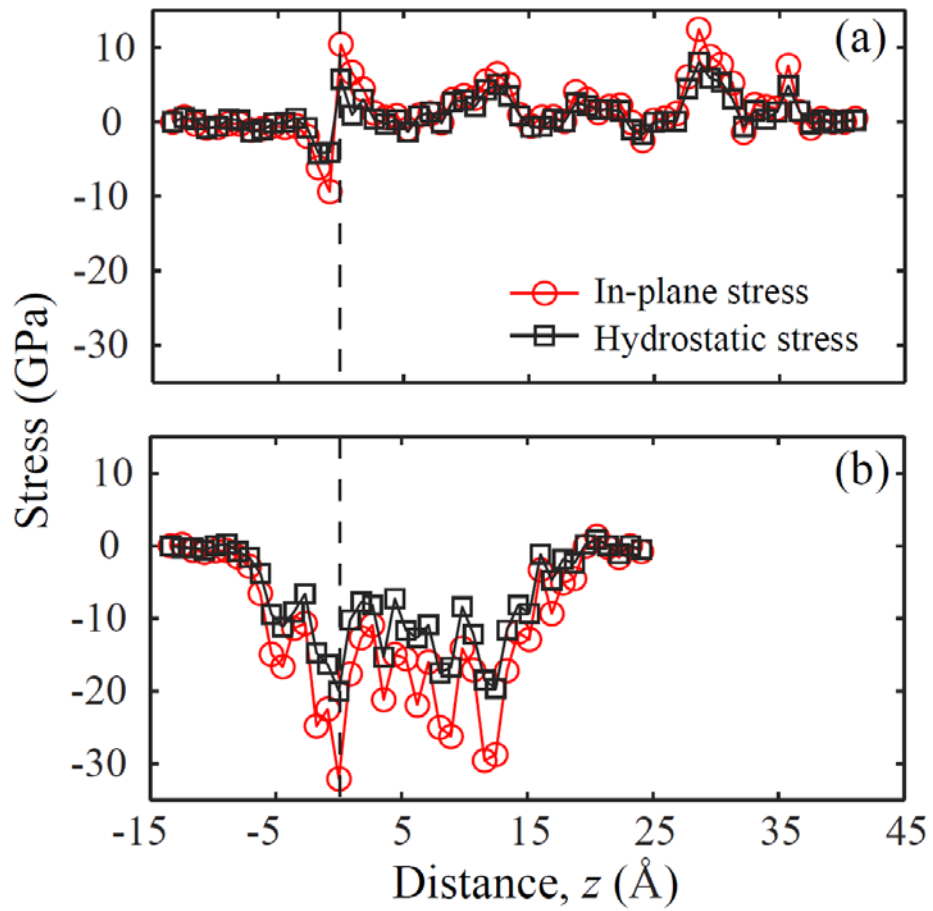


**Figure 10**

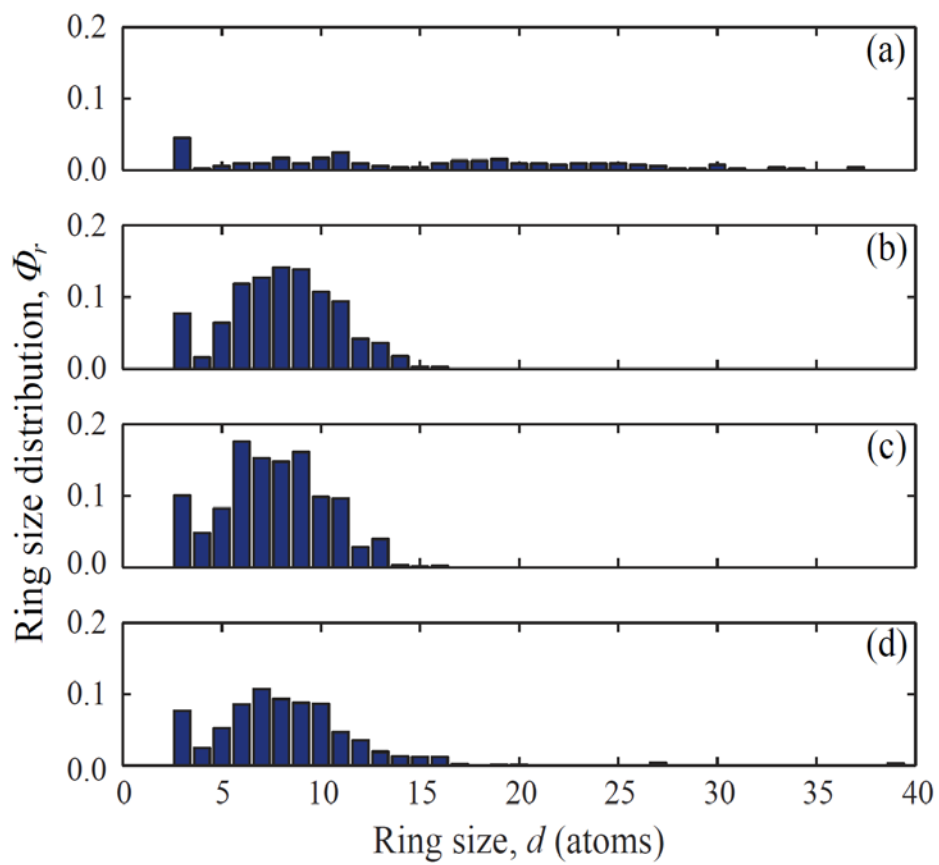


**Figure 11**

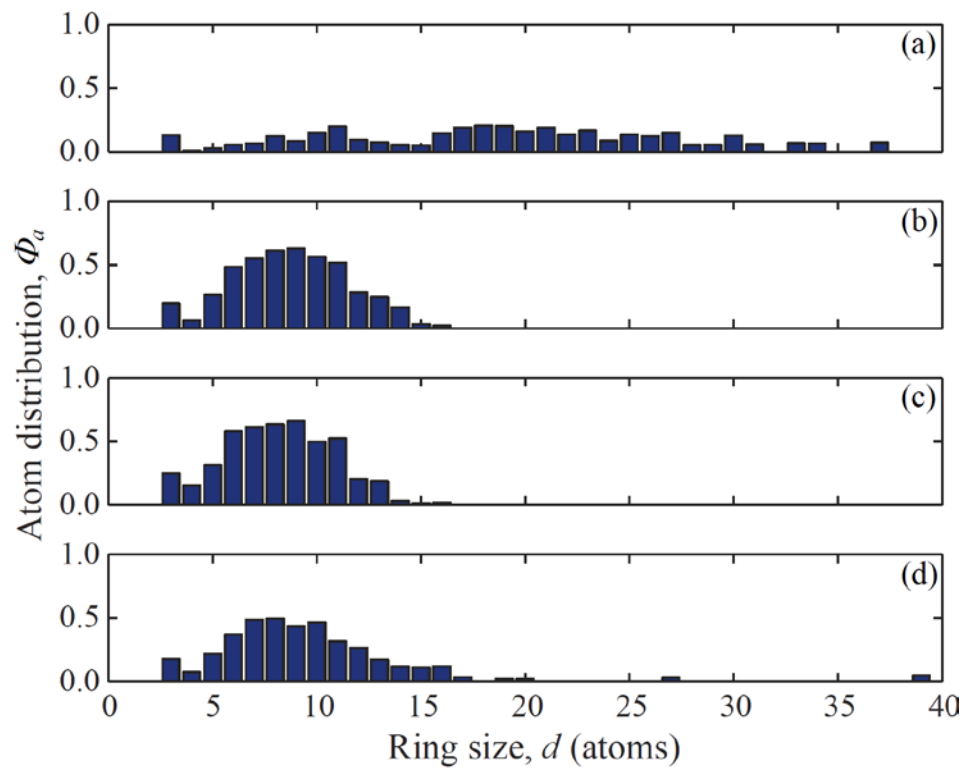


**Figure 12**

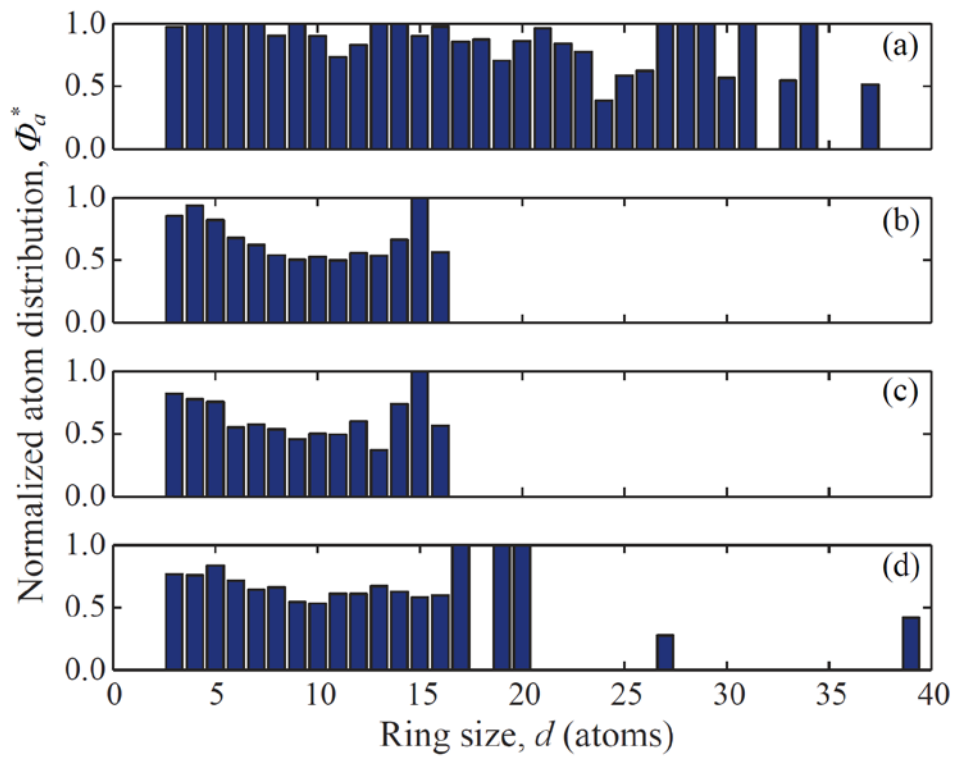


**Figure 13**

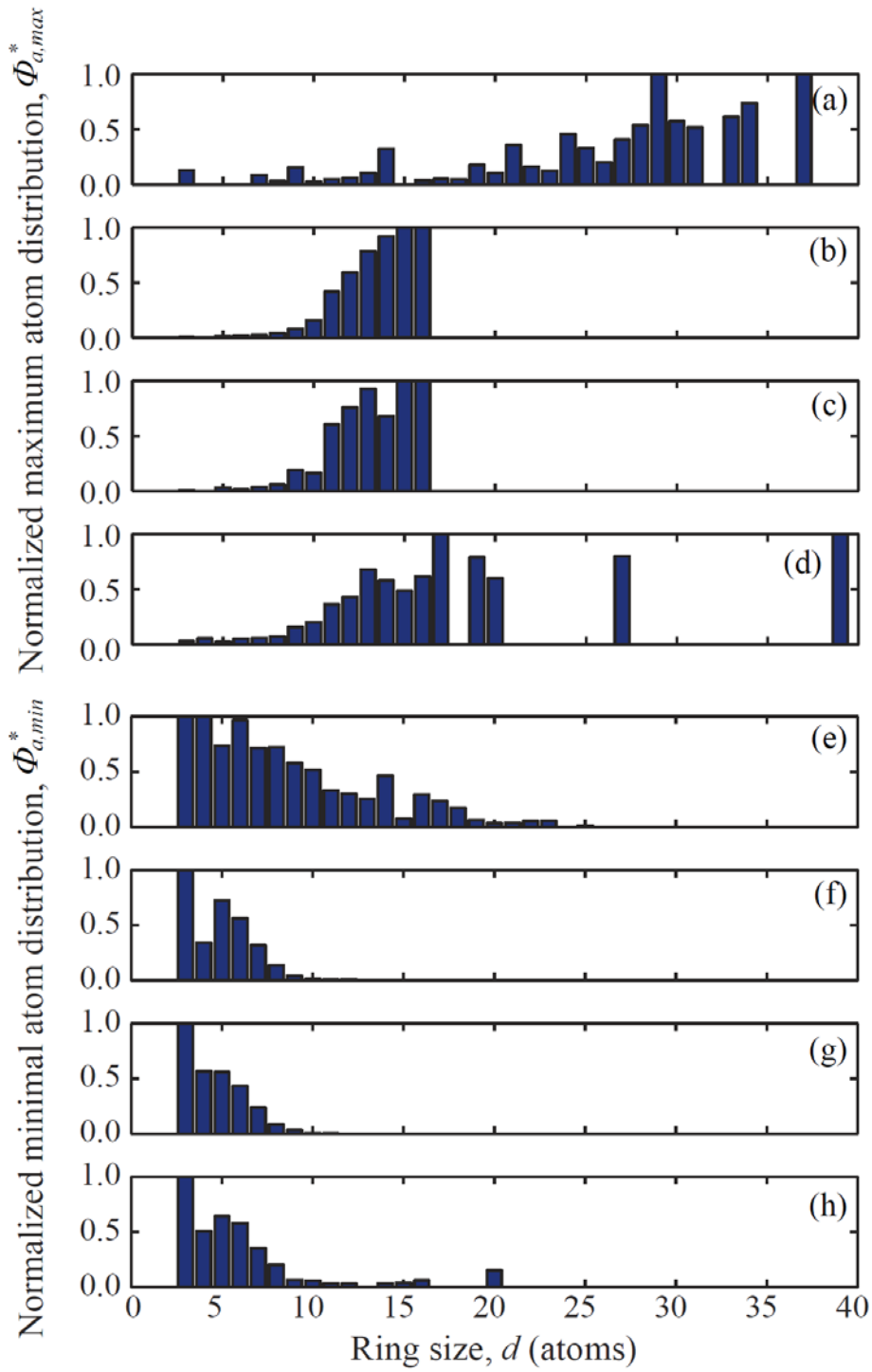


**Figure 14**